CrossMark

Qualitative Assessments via Infrared Vision of Sub-surface Defects Present Beneath Decorative Surface Coatings

Stefano Sfarra[1,2,4,5] · Henrique C. Fernandes[3] · Fernando López[4] · Clemente Ibarra-Castanedo[4] · Hai Zhang[4] · Xavier Maldague[4]

Abstract In this work, the potentialities of the infrared vision to explore sub-superficial defects in polychromatic statues were investigated. In particular, it was possible to understand how the reflector effect of the exterior golden layers could be minimized, applying advanced statistical algorithms to thermal images. Since this noble metal is present as external coating in both artworks, an in-depth discussion

✉ Stefano Sfarra
   Stefano.Sfarra@univaq.it

   Henrique C. Fernandes
   henrique.fernandes@ufu.br

   Fernando López
   fernandol@irthermalvision.com

   Clemente Ibarra-Castanedo
   IbarraC@gel.ulaval.ca

   Hai Zhang
   hai.zhang.1@gel.ulaval.ca

   Xavier Maldague
   Xavier.Maldague@gel.ulaval.ca

[1] Las.E.R. Laboratory, Department of Industrial and Information Engineering and Economics, University of L'Aquila, Piazzale E. Pontieri no. 1, 67100 Monteluco di Roio, L'Aquila (AQ), Italy

[2] Tomsk Polytechnic University, Lenin Av., 30, Tomsk, Russia 634050

[3] Department of Computer Science, Federal University of Uberlândia, 2121 Av. Joao Naves de Avila, Uberlândia 38400-902, Brazil

[4] Computer Vision and Systems Laboratory, Department of Electrical and Computer Engineering, Laval University, 1065, av. de la Médecine, Quebec City G1V 0A6, Canada

[5] INFN CHNet, Laboratori Nazionali del Gran Sasso, Via G. Acitelli 22, 67100 Assergi, L'Aquila (AQ), Italy

concerning its physicochemical properties is also added. In this context, the principal component thermography technique and, the more recent, partial least squares thermography technique were used on three different datasets recorded, providing long thermal stimuli. The main images were compared both to phasegrams and to the thermographic signal reconstruction results in order to have a clear outline of the situation to be debated. The effects of view factors on the radiation transfer linked to the specular reflections from the surface did not falsely highlight certain features inadvertently. Indeed, the raw thermograms were analyzed one by one. Reflectograms were used to pinpoint emissivity variations due to, *e.g.*, possible repainting. The paper concludes that, as it is possible to understand from a physical point of view, the near-infrared reflectography technique is able to examine the state of conservation of the upper layers in cultural heritage objects, while the infrared thermography technique explores them more in-depth. The thesis statement is based on the thermal and nonthermal parts of the infrared region, therefore, indicating what can be detected by heating the surface and what can be visualized by illuminating the surface, bearing in mind the nature of the external coating.

1 Research Aim

The state of conservation of gilded coatings is of paramount importance in the cultural heritage (CH) field. The use of the infrared thermography method may be a good option in this case since it is safe, nonintrusive, and noncontact, allowing the detection of relatively shallow subsurface defects. Unfortunately, raw thermograms suffer from unwanted reflections when materials having low emissivity values, such as Gold, are under inspection. However, image processing by statistical algorithms substantially reduces this effect, facilitating diagnosis. The combined use of visual inspection and near-infrared detectors are, however, highly desirable in this task. In the present research work, two ancient statues chiseled on different supports were inspected, taking into account a preliminary rigorous discussion inherent in the physical concepts of this matter.

2 Introduction

The surface of polychrome artifacts is the first interface that an art object offers for study and monitoring during diagnosis or preventive conservation campaigns. The structure and composition of this interface are often complex, which is a clear indication of their history and potential previous interventions. The interface also indicates the influence of other components of the polychrome layers and of the support itself on the surface pattern and conservation state [1]. The first and most stable material for creating precious objects or gilded surfaces was gold. *E. Hecht* and *A. Zajack* explained in detail in theirs Optics textbook (1974) why gold, a noble metal, actually "reflects, or better stated creates" "gold" color [2]. Since ancient times, gold was selected for

its properties, *i.e.*, golden shine and glitter, resistance to corrosion (it is the most electronegative transitional element), and rarity. Its face-centered cubic crystal structure makes it soft and ductile, which together with its chemical stability, led to the use of gold as in the form of gold leaves and powder to cover various objects [3–6].

The arrangements of outer electrons, the nature of its color, the conditions for the intense absorption of light at the wavelengths necessary to produce the typical gold color, its density, its ability to efficiently transfer heat and electricity, its electrical resistivity, thermal conductivity, corrosion resistance, and electrode potential are all technical characteristics explained in [7].

Metallic pigments are used for the aesthetic properties they lend to coating systems. Each metallic pigment grade offers a slightly different appearance property to these coatings, and it is necessary to be able to access these differences. Some of the most important properties to take into account are: the *face-color*, or *head-on-brightness*, the *flop*, *flip/flop*, or *metallic travel angle*, the *Seed level*, the *DOI (distinctness of image)*, the *Patina*, and the *color* [8]. As soon as the first coating layer has been surpassed, the thermal conduction inside the solid becomes prevalent. The thermal conduction effect is not taken into account in the study of the results coming from the near-infrared reflectography technique, since in this case the portion of the wavelengths reflected by the surface becomes prevalent.

The fundamental relation which correlates the thermal flux to the gradient of the temperature based on experimental observations is the Fourier Law. It is enucleated as Eq. 1.

$$\dot{q} = -K\nabla T, \tag{1}$$

where the gradient of the temperature is a vector normal to the isothermal surface, while the thermal flux vector $\dot{q}(\mathbf{P}, \theta)$ is the thermal energy that flows in the unit of time per unit area of isothermal surface in the direction of the decreasing temperatures, and k is the thermal conductivity of the material expressed in $W \cdot m^{-1} \cdot K^{-1}$ [9]. From Eq. 1, it is possible to deduce that being equal the thermal gradient (*i.e.*, the cause), the thermal flux (*i.e.*, the effect) is greater if the conductivity of the medium is bigger. The latter is a physical property of the material, which characterizes the aptitude to the thermal conductivity exchange; it depends on the chemical composition (Fig. 1), on the structure, and on the phase. The order of magnitude for k varies into a very large interval. The thermal conductivity value of gold in the solid phase was quantitatively studied by Petrov *et al.* in 2015 [10].

In this work, two polychromatic ancient statues were investigated by using infrared vision, *i.e.*, near-infrared reflectography (NIRR), and infrared thermography (IRT) methods [11,12].

The first one is named *Madonna sitting on the throne with Child* (first decade of sixteenth century) inherent in the polychromatic and gilded art based on terracotta support [13]. The clarification regarding the masterpiece's creation is still a moot point. It is currently attributed to the art master *Magistro Silvestro Jacobi de Turri* or his pupil *Saturnino Gatti* [14]. The statue, which resisted the 2009 quake, was damaged on the lower part, ironically during the 35th G8 summit held in L'Aquila in 2009 [15]. A thermographic analysis was performed on the same object in order to detect subsurface defects caused by the soil impact.
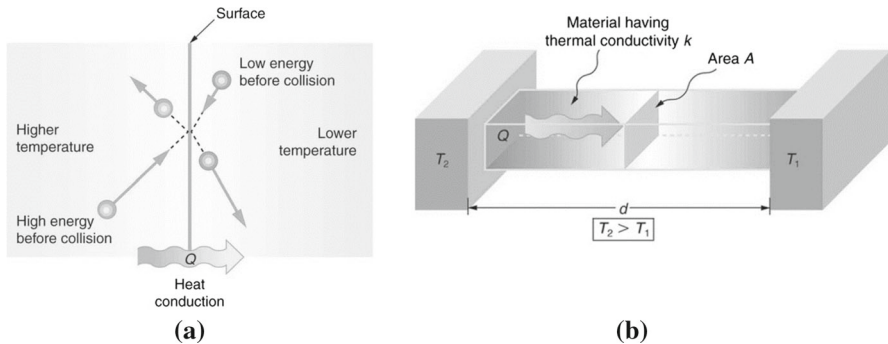
Fig. 1 Microscopic illustration of conduction: (a) The relationship between molecules—collisions—heat conduction through two adjacent mediums is illustrated, and (b) the effect of thickness on heat conduction is schematized

Currently, it is preserved at the National Museum of Abruzzo (Munda) located in L'Aquila (Italy) [16].

The second statue represents *Saint Equizio* (height: 68 cm), protector of the city of L'Aquila (Italy). It is a half-length and round bust sculpted on a wooden support. It is attributed to *Pompeo Cesura*. According to the *Verlengia*'s theory, probably it is the only sculpture of the famous art master. It was conceived in the sixteenth century, while the restoration was performed in 1967 [17]. In 2011, *i.e.*, after 44 years, a thermographic inspection was carried out with the intent to understand the state of conservation of the artwork, while a near-infrared reflectography (NIRR) analysis focused on the detection of repainting was also conducted as part of an integrated nondestructive campaign.

In practice, this work is focused on two artworks having a golden external layer and two different supports. Similar experiments conducted in the past can be found in [18] for the terracotta support, and in [19] for the wooden support.

IRT data were processed by means of two statistical algorithms, *i.e.*, principal components (PC) and the partial least squares regression (PLSR) [20]. In particular, the analysis of PCs involves a mathematical procedure that transforms a number of possibly correlated variables into a smaller number of uncorrelated variables. The first principal component accounts for as much of the variability in the data as possible, and each succeeding component accounts for as much of the remaining variability as possible. In the thermographic field, the data analysis linked to PCs is called principal component thermography (PCT) [21].

To the best of our knowledge, the PLSR was used in the thermography context linked to the cultural heritage field, for the first time, in 2014 [22,23]. In this case, the thermographic analysis combined with the PLSR algorithm is called partial least squares thermography (PLST) technique [24].

In addition, the pulsed phase thermography (PPT) [25] and thermographic signal reconstruction (TSR) [26–28] also provided interesting results when applied on the same dataset.
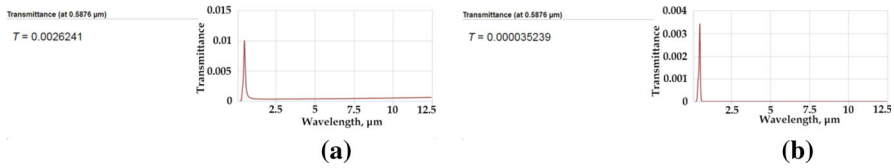
Fig. 2 Transmittance of Au (gold) at 0.5876 μm: (a) transmittance curve at 100 nm, and (b) transmittance curve considering multiple reflections and ignoring the interference

In both cases, a LWIR camera (FLIR S65 HS, 320 × 240 pixels, 7.5–13 μm) along with one 2 kW IR lamp (STAR projects) which provided long square pulses were used. IRT data were processed using a software named IR View [29].

The results show that PLST and PPT can greatly reduce the influence of the pictorial layers, *i.e.*, the emissivity variations from different pigments. The restorer can therefore work together with the diagnostician during the analysis of gold coatings via infrared vision [30] in order to understand the state of conservation of statues or artistic objects.

3 Technical Notes on the Golden Layers in the Cultural Heritage (CH) Field

It should be noted that if a metal has a particular color, it is indicative of the fact that the atoms are partaking of selective absorption by way of the bound electrons. This is in addition to the general absorption characteristic of the free electrons. It is important to remember that if a medium that possesses strong absorption at a particular frequency, it reflects the nonabsorbing part of the incident radiation [31,32].

Gold and copper are reddish yellow because n_I increases with wavelength and the larger values of λ are reflected more strongly as explained in [2]. Thus, *e.g.*, gold should be fairly opaque reflective at longer visible wavelengths. Consequently, under white light illumination, a gold foil less than roughly 100 nm thick will indeed transmit predominantly greenish-blue light and reflect most of the yellow, orange, and red. This is true for internal transmission only (Fig. 2a). The transmittance increases if the multiple reflections (ignoring the interference) are considered (Fig. 2b) [33].

These graphs have been studied *ad hoc* following [34]. They fit the experimental data from several sources with the Brendel–Bormann (BB) model. They can be considered adaptable in the cases treated herein, since they refer to an external thickness of gilded gold usually applied at that time [35]. Multiple reflections are considered since the inspected statues have concavities that can amplify this effect.

Most often the index of refraction for a metal will be complex, and the impinging wave will suffer absorption in an amount which is frequently dependent.

Figure 3 illustrates the spectral reflectance at normal incidence for a number of evaporated metal films under ideal conditions. On the one hand, it should be noted that gold (Au) reflects mostly in the yellow spectrum and above (> ~ 590 nm). On the other hand, silver (Ag) is highly reflective across the whole visible spectrum (and beyond); it is semitransparent in the ultraviolet at about 316 nm and below.
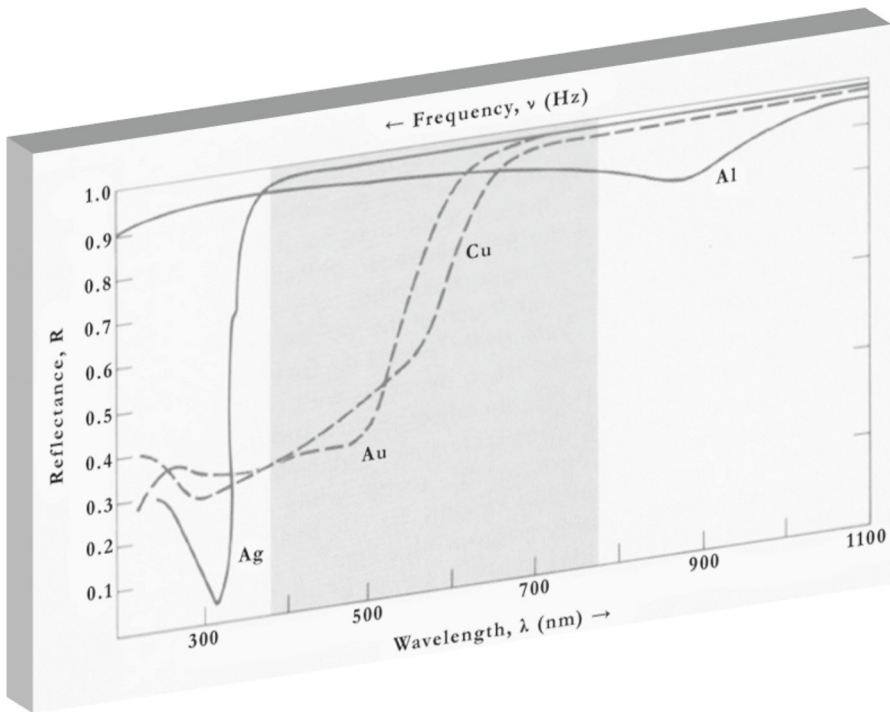
Fig. 3 Reflectance versus wavelength for silver, gold, copper, and aluminum (adapted from [2])
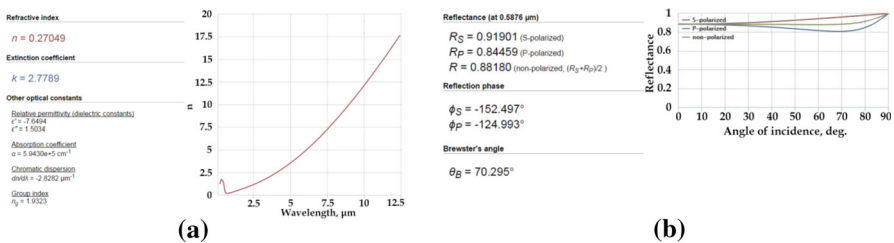

Fig. 4 (a) Refractive curve and (b) reflectance curve at 45° with an in-going direction

The most interesting part of the Au curve is drawn in Fig. 4a. It refers to refractive index and explains the optical constants (relative permittivity, absorption coefficient, chromatic dispersion, and group index) of Au (Gold), along with the reflectance, reflection phase, and Brewster's angle for an angle of incidence of light of 45° (Fig. 4b).

The mechanism responsible for the yellowish-red hue of gold and copper is, in some respects, similar to the process which causes the sky to appear blue. In practice, the molecules of air have resonances in the ultraviolet and will therefore be driven into larger amplitude oscillations as the frequency of the incident light increases toward the ultraviolet. Consequently, they will effectively take energy from and reemit (*i.e.*, scatter) the blue component of sunlight in all directions, transmitting the complementary red end of the spectrum with little alteration. This is in analogy with the selective

reflection or scattering of yellow–red light that takes place at the surface of a gold film and the concomitant transmission of blue–green light. In contradistinction, the characteristic colors of most substances have their origin in the phenomenon of selective or preferential absorption [2]. It is possible to conclude that, in the final stage, the blue color of the sky is caused by the scattering of sunlight off the molecules of the atmosphere. This scattering, called *Rayleigh* scattering, is more effective at short wavelengths (the blue end of the visible spectrum). In addition, the light scattered down to the earth at a large angle with respect to the direction of the sun's light is predominantly in the blue end of the spectrum. The scattering at 400 nm is 9.4 times as great as that at 700 nm for equal incident intensity.

Different materials are used during the gilding process. Among these, there are:

– The gold leaf: It is obtained by hammering between two thicknesses of leather that make it very thin and handy;
– Bologna gypsum (also called *Meudon* white): It is hydrated calcium sulfate. It is soft to the touch, given its grain. It should never be boiled to prevent the formation of clumps that are detrimental to the plastic compactness of the final product. It should therefore be dissolved in a bain-marie. It is finally stored in a dry place because it fears the moisture.
– Rabbit glue (also called *Lapin* glue): It is obtained from the rabbit skin immersed in a bath of limewater. It was also known before the fabrication of the carpenter's hot glue (also available as liquid animal glue ready-to-use) and, if compared to the latter, it has a lower tenacity. This makes it ideal for the plaster procedure. It needs to be dissolved in bain-marie (100 g of glue in 1 l of water) in order to obtain the required mixture for plaster and bolo preparation. It should be used warm but not hot.
– Fish glue: It is derived from the bladder of a few species of fishes, such as sturgeons and similar. It is marketed in the form of flakes, which should be left in water for about 24 hours before the use. After the decantation of the excess of water, the glue is dissolved in a bain-marie. If compared to the other glues, it does not increase a lot its volume. It is used to put in contact the golden leaf with the bolo.
– Armenian bolo: It will be described in Sect. 7.

As mentioned above, gold absorbs the blue–green bands of white light and reflects the yellow–red spectral bands; therefore, the light is depleted of green and blue. For example, the colored pigments make use of transition metals, whose internal orbitals are not all filled with electrons, and thus exhibit absorption bands in the visible spectrum. Among these, it is possible to find lead chromate, *i.e.*, the yellow chromium.

Generally, substances that have higher refractive indices are linked to greater opacity values; this effect is also named *covering power*. This explains the difference between yellow pigments and gold layers.

The higher the refractive index of the pigment relative to that of the medium and the nearer the particle size to the optimum, the greater the scatter and the greater the opacity of the paint. The hiding power of a paint containing a colored pigment is also dependent on the ability of the pigment to absorb light, as well as to scatter it as a result of its refractive index and particle size distribution. All inorganic pigments have high refractive indices, and hence, when used to color, paint give high opacity. Such

colors from inorganic pigments generally include white, black, and yellow, red and green oxides.

This explains the fact that in the yellow area, where less amounts of light are absorbed, the predominant mechanism for achieving hiding power is light scattering. It is for this reason that inorganic pigments (refractive index around 2.5–3) such as chrome yellows when used alone have a significantly higher hiding power potential than organic pigments (refractive index around 1.6–2) due to their higher scattering effect. However, the additional color strength imparted by organic pigments means that they can be blended with other hiding power inorganic pigments (titanium dioxide, iron oxides, *etc.*) to give an acceptable hiding power. Blending with pigments such as TiO$_2$ is probably the best known technique for achieving hiding power; however, it should be noted that other pigments offer the potential to reduce light penetration by the mechanism of absorption. For example, the achievement of hiding power using an organic red can be greatly enhanced if a small quantity of carbon black can be tolerated in the shade required. The very high level of light absorption given by the carbon black can offset the relatively low absorption/scattering of the organic pigment. It is in this regard that the cleaner the color and the higher the level of color saturation that is given by the major color component in the formulation, the greater the flexibility to tolerate other pigments that can enhance hiding power due to light absorption [36].

Therefore, the value of the refractive index varies for different orientations of the light to the crystallographic axes of crystal materials. In fact, the pigment crystallites in paint are randomly oriented with respect to one another [37].

4 Thermographic and Reflectographic Techniques

The remainder of the article is divided into three main parts. Firstly, this section is divided into five subsections which explain to the reader the relevant theoretical background inherent in the post-processing techniques applied herein, while the second part describes the NIRR equipment and its main principles. Finally, the last section summarizes the main findings.

PLST technique is briefly described in Sect. 4.1 since it has recently been introduced into the scientific panorama.

4.1 Partial Least Square Thermography (PLST) Technique

The use of the partial least square (PLS) method applied to thermographic data is fully explained in [24]. The authors followed the latter scientific reference, as well as the use of the PLS regression (PLSR) applied to square pulsed thermography (SPT) data in order to obtain the results shown in Sect. 7. The thermal images obtained during the SPT inspection are typically arranged into a 3D matrix, whose x and y axes are represented, respectively, by i and j pixels, while the z axis corresponds to the k frame number. N_x and N_y correspond to the total number of pixels along the x and y directions, while N_T is the total number of frames. A schematization of this process is shown in Fig. 5.
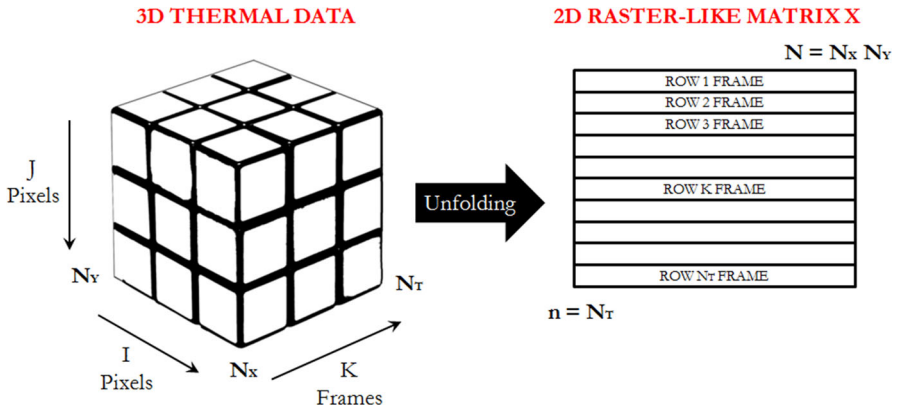
Fig. 5 Schematic representation of the transformation of the 3D thermal data into a 2D raster-like matrix
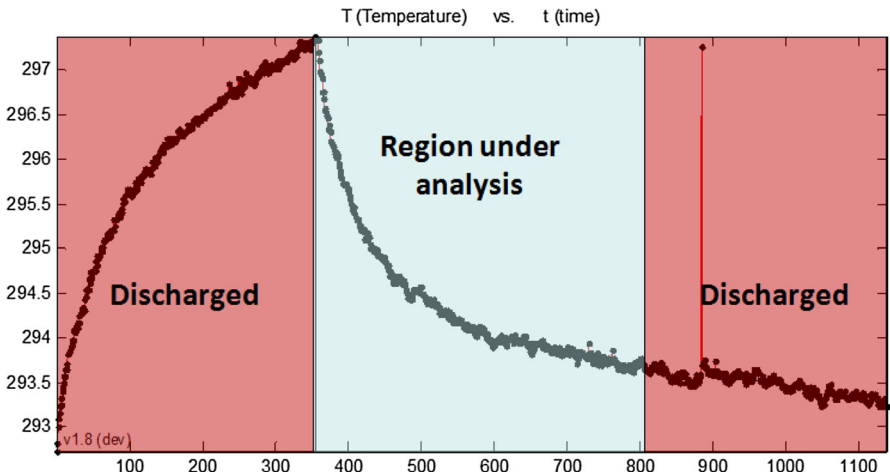

Fig. 6 Heating and cooling phases of the particular of *Saint Equizio* polychromatic wooden statue

As can be seen from this figure, the first step consisted in the transformation of the 3D thermal data into a 2D raster-like matrix. This process is known as unfolding. For the following steps, the readers can refer to [22,23].

Data used in this study, useful to investigate the applicability of PLSR, are based on a part of the thermal sequence obtained from the SPT inspection, and named *region under analysis* (Fig. 6). The 3D sequence ($320 \times 240 \times$ *region under analysis*) is mean-centered and converted into a 2D raster-like matrix X. The predicted Y matrix is a column vector composed of a time series. For more explanations concerning this mathematical concept, please refer to [38].

In the Saint Equizio's case study, the region of the cooling down phase analyzed via PLST technique is highlighted with a light blue color in Fig. 6. However, the whole sequence was useful during analysis via PCT technique.

In Sect. 7, readers can also find the PCT, PPT, and TSR results that show the need to utilize different algorithms when the inspection of polychromatic objects is carried out by using the infrared spectrum. A brief summary of their physical concepts is explained in the following.

4.2 Principal Component Thermography (PCT) Technique

PCT, originally proposed by Rajic in 2002, extracts the image features and reduces undesirable signals. It relies on singular value decomposition (SVD), which is a tool to extract spatial and temporal data from a matrix in a compact manner by projecting original data onto a system of orthogonal components, known as empirical orthogonal functions (EOF). The first EOF will provide the most important characteristic variability of the data; the second EOF will provide the second most important variability, *etc*. Original data can be often adequately represented with only a few EOFs. Usually, an infrared sequence of 1000 images can be replaced by 10 or less EOFs [21].

4.3 Pulsed Phase Thermography (PPT) Technique

PPT allows retrieving phase and amplitude data also from a SPT experiment. This method can be thought as being a combination of pulsed thermography (PT) and lock-in thermography (LT). In a similar manner as for LT, phase data are commonly analyzed since they are more tolerant to the nonuniform heating and environmental reflections [25]. In particular, the surface temperature is monitored using an infrared camera after the heating phase ($T(t)$). Then, the discrete Fourier transformation is applied to ($T(t)$), leading to phase as a function of frequency ($\varphi(f)$) using Eq. 2:

$$\varphi(f) = \tan^{-1} \frac{I(f)}{R(f)} \tag{2}$$

Therein, f stands for the frequency, and $R(f)$ and $l(f)$ are real and imaginary components obtained using the Fourier transform. In PPT, phase images for each frequency are constructed using $\varphi(f)$. Subsurface defects are detected by observing the phase difference between defective and nondefective surfaces ($\Delta\varphi$) in the phase images.

4.4 Thermographic Signal Reconstruction (TSR) Technique

TSR processing technique has originally been developed for PT, and it is widely applied in nondestructive testing (NDT) and evaluation (NDE). An in-depth explanation of this very interesting technique can be found in [26–28].

4.5 Near-InfraRed Reflectography (NIRR) Technique

By operating technical changes in digital cameras, companies specialized in products for astronomy are able to offer devices dedicated to inspection in the ultraviolet and

the infrared spectra. Among them exists the Canon 40DH spectrum enhanced with the internal filter named EOS045, wideband spectral and EF55-200 lens of the same company, also equipped with a CMOS sensor 22.2×14.8 mm having 10 megapixels ($5.7\,\mu$m pixel pitch). In order to obtain the EOS 40DH, the substantial change consisted in the removal of the anti-IR filter, as well as in the subsequent positioning of the Idas Clear/AR filter. Adapting to the geometry of the sensor, this filter allows proper autofocus by simultaneously avoiding the internal reflections effect. In addition, by transmitting all wavelengths between 380 nm and 1000 nm, the Idas Clear/AR filter makes the Canon EOS 40DH a suitable tool for the reflectographic acquisitions, when a suitable filter is placed in front of the camera lens by excluding the visible radiation. The possibility to perform infrared acquisitions is compatible with the manual setting of other functions, such as the white balance, the opening of the stop, and the variation of the exposure times.

The lighting of the statues was carried out by using the same lamp also used in thermographic inspection. During the reflectographic measurements, a band-pass filter working at 680 nm was mounted on the external lens of the camera [39]. Among the filters currently available in the Las.E.R. Laboratory (L'Aquila, Italy), the 680 nm was chosen by taking into account the graphs shown in Figs. 3 and 4a. In practice, the minimization of the effect of the reflectance (R) was reached, since Au has a minimum peak around 500 nm. Therefore, no additional filters mounted on the external lens of the camera were used. Indeed, imaging can be concentrated into narrow-wavelength bands, such as a range near to 1100 nanometers (nm) that is useful for the visualization of brownish inks, which is transparent at this wavelength. Otherwise, it can be applied around $2\,\mu$m for the penetration of particular opaque paints, such as malachite green.

The art masters of the time considered three parameters for obtaining a correct paint formulation with no knowledge of the Kubelka–Munk theory, which is strictly connected with the NIRR technique [40]. These parameters include the pigment load, thickness, and opacity or hiding. The art masters also considered the correct pigment/binder ratio, critical volume concentration (CPVC), and weight/liter. The two-constant (K and S) theory predicts the characteristic properties (K- absorbance and S-scatter) of pigments by simply measuring color in terms of reflectance. On the one hand, the role of white pigment is to scatter (S) and give opacity. On the other hand, the role of black pigment is to absorb (K) and give opacity. The role of colored pigment is to mainly absorb (K). In addition, some of the high-chroma yellow and red pigments not only absorb the light but they also scatter the light to a large extent and behave like white pigment. Opacity, which is directly related to contrast ratio (CR), can be determined by measuring the paint sample applied on the Morest or Leneta Chart (paper with black and white stripes). The ratio of reflectance over the black portion (R_B) and reflectance over the white (R_W) portion directly indicates the CR as a ratio (R_B/R_w). As the opacity increases with thickness, it is possible to achieve proper hiding for the required thickness.

For the application of the Kubelka–Munk theory, an opaque material is needed. Reflectivity is the reflectance of such a layer which is so thick that it is opaque. That is, if the thickness is increased, no further change is observed.

Generally, the full opacity is achieved at CR = 0.98. The hiding power of paint is understood to be its ability to eliminate the contrast between a black substrate and a

white substrate to the extent that the reflectance obtained over a black substrate is 98 % of that obtained over a white substrate. The mathematical formulation of the theory can be found in [40].

5 Description of the Madonna Sitting on the Throne with Child

The dimensions of the *Madonna sitting on the throne with Child* are: 193 cm in height, 106 cm in width, and 87 cm in depth. Additional information regarding the fabrication of similar statues, as well as the restoration phase of inspected statue, can be found elsewhere [41–43].

The thermographic analyses were focused on two different parts located on the left side of the mantle. In particular, Table 1 summarizes the main information inherent in the thermographic campaigns (L = lamp, T = thermal camera and A = artwork).

6 Description of the Saint Equizio Polychromatic Wooden Statue

The statue of Saint Equizio is represented with a beard and in a monastic suit. In the raised left hand, he should have had the crosier (currently lost) alluding to his position of abbot.

The thermographic analysis was focused on the front side of the half bust. In particular, Table 2 summarizes the main information inherent in the thermographic campaign (L = lamp, T = thermal camera, and A = artwork).

7 Results and Discussion

The infrared vision inspections were performed in the Laboratory of the Musè Il Museo delle Paludi di Celano, Italy, after preliminary restoration works. In particular, the authors centered their attention on two different regions of interest (ROI), located on the left side by looking at the face of the statue. The first upper part is illustrated in Fig. 7, while the second lower part is shown in Fig. 8.

As shown in Fig. 7a, the *Madonna* has a golden mantle. The infrared vision inspection was applied on this part. The NIRR analysis (Fig. 7b) shows a darker zone on the right shoulder that could be attributed to an ancient restoration, maybe a pictorial retouching. It is surrounded by an irregular dotted red line in order to clarify the position. In particular, one notes the presence of the red bolo, also known as Armenian bolo, which is composed of kaolin containing iron dioxides. It has a natural origin and has been used since the Middle Ages. It was not always used as pigment; however, when it was mixed with dilute solutions of glue, it was applied on plaster as a homogeneous and fine background for gilding in gold leaf. In fact, its structure allows an excellent polishing.

Figure 7c–h reveals the repaired parts of the mantle of the *Madonna*, which appear either as white (Fig. 7c–d, f–g) or dark (Fig. 7e, h) spots depending on the algorithm applied. It is important to notice that these spots appear at the early stage of the

Table 1 The main measurement conditions of the IRT setups of the *Madonna sitting on the throne with Child*

Setup	Period	Distance between L and A (m)	Distance between T and A (m)	Sampling frequency (f_s) (Hz)	Number of lamps	Heating time (s)	Cooling time (s)	Ambient temperature (°C)	Relative humidity (%)
Upper part	2011	1.88	1.79	1	1	300	659	17	39.1
Lower part	2011	1.64	1.97	1	1	360	780	16.1	41.8

Table 2 The main measurement conditions of the IRT setups of the *Saint Equizio* polychromatic wooden statue

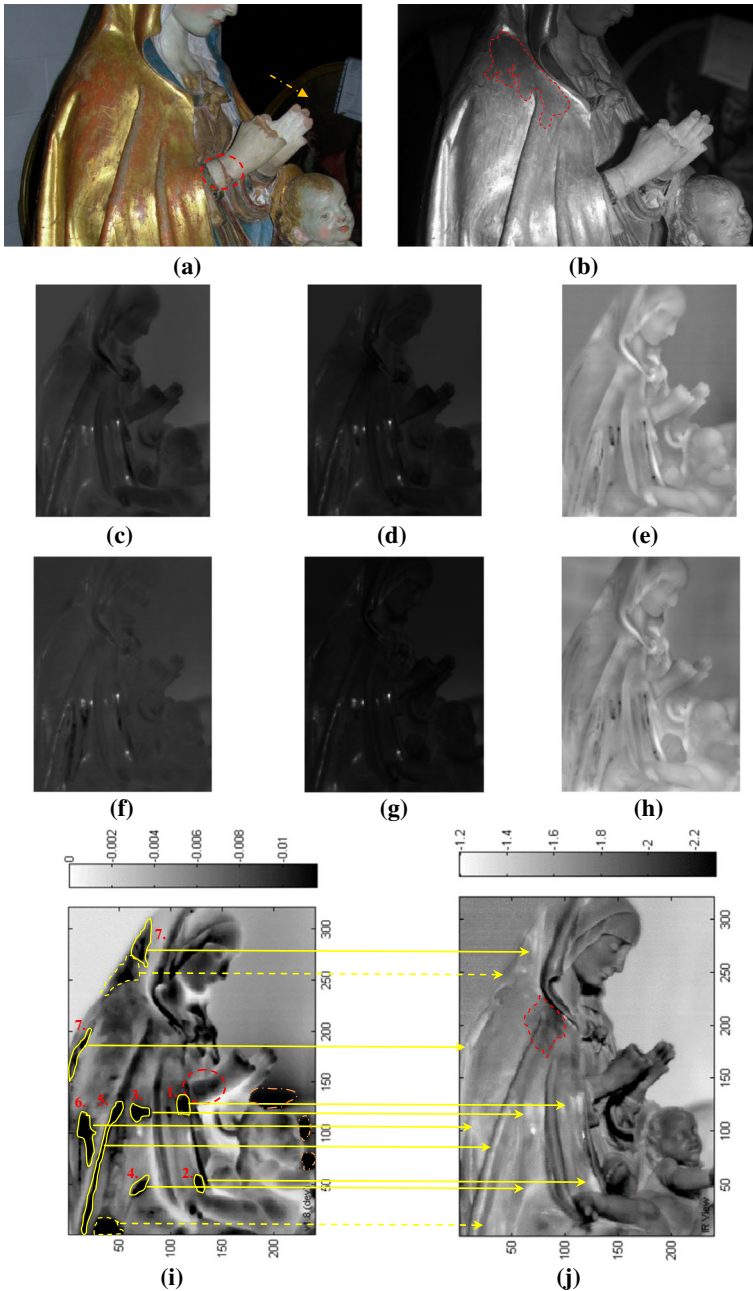| Setup	Period	Distance between L and A (m)	Distance between T and A (m)	Sampling frequency (f_s) (Hz)	Number of lamps	Heating time (s)	Cooling time (s)	Ambient temperature (°C)	Relative humidity (%)
Front side	2011	1.77	2.17	1	1	120	360	9	35.7

Fig. 7 Our Lady in polychromatic terracotta (half-length): (a) Photograph, (b) Reflectogram at 680 nm, (c) Regressed thermal sequences (all components)—30th image, (d) Nonuniform heating suppressed (1st component suppressed)—30th image, (e) Regressed thermal sequences (all components)—360th image, (f) Nonuniform heating suppressed (1st component suppressed)—360th image, (g) 2nd EOF–PCT, (h) 3rd EOF–PCT, (i) TSR, 4th degree, 1st derivative, and (j) PPT, phasegram at $f = 0.0010428\,\text{Hz}$
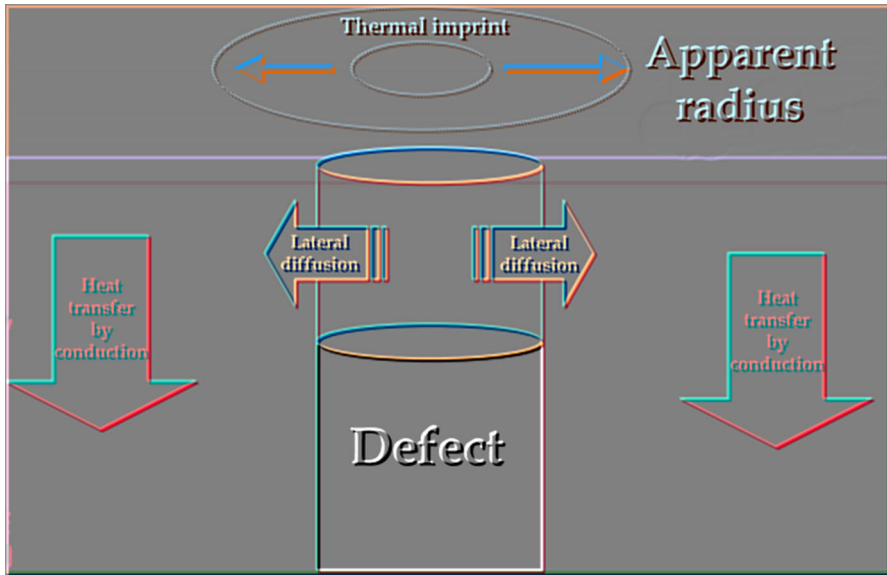
Fig. 8 Direction of the thermal conduction and apparent radius of a sub-superficial defect greater than the real size

heating phase. They are not correlated with environmental reflections, considering the refractive index (Fig. 4a) and the reflectance graphs (Fig. 4b) connected to the position of the lamp installed at 45°. Figure 7i shows the presence of wider damages; many of these are located on the same areas in which the white spots appear in Fig. 7j. In fact, although the 1st derivative image showed considerable enhanced contrast with respect to the raw thermograms, additional subsurface information can be recovered with the phase [44]. In Fig. 7i, the defects confirmed with the phase analysis are surrounded by yellow irregular solid lines (also linked via solid arrows to the same positions of Fig. 7j), while the nonconfirmed defects to be studied as future perspectives with other NDT methods are surrounded by yellow irregular dotted lines (also linked via dotted arrows to the same positions of Fig. 7j). In addition, defects 1.—7. are also slightly detectable in Fig. 7c, d, f, g. It is possible to see that, in this case, TSR technique is able to reveal thermal inhomogeneities also on a painting on canvas positioned on the back of the scene of interest (Fig. 7a). For a sake of clarity, they are surrounded by brown dash dot irregular lines (Fig. 7i). Detection of thermal inhomogeneities on the back of the region of interest (ROI) has already been pointed out in [45]. This can be due to the reduction of: (a) the background noise, (b) the onset time, and (c) the time of maximum signal contrast of the defects, which consequently reduces the blurring effect [46].

This is an important clue which is at the base of the apparent radius concept and defect sizing [12]. Firstly, the overpaintings are detectable in the first step as explained in [47], secondly, the defect "emerges" on the surface in the second step, by following the thermal conduction concept, the lateral diffusion process (Fig. 8) and the combined thermal diffusivity [48] parameter linked to the upper layers.

The lateral heat diffusion problem and the blurring effect are explained in depth in [49]. In this work, it is explained how considering the 3D heat diffusion problem in anisotropic media, the Fourier number can be written for each direction (x, y, and z).

It depends on the thermal diffusivity along the x-, y-, and z-directions. It also explains how the degradation of signal—or blurring—takes place when the heat diffusion in the x- and y-directions becomes predominant.

In practice, the deeper defects (or those with smaller aspect ratio) are suffered more the blurring effect. From the equations shown in the latter work, it is possible to see how the thermal diffusivity parameter plays an important role during the inspection of anisotropic materials, such as multilayer structures (polychromatic statues, mural paintings, *etc.*). This is also the case of the detection of the defects on the back of the scene, *i.e.*, the defects linked to the painting on canvas (Fig. 7a—see the yellow arrow), usually formed by several layers [50].

Of great interest is the detection of the damage on the right wrist (Fig. 7i), that is presumably more extended in depth with respect to the visible damage of Fig. 7a. The latter certainly correspond to an ancient restoration [41]. On the right wrist of the Madonna—which is surrounded by a red dotted oval in Fig. 7i, the influence of the gilded coating during the thermographic recording is not present. In fact, this part of the statue was realized by clay covered by a thinner layer of plaster (Fig. 7a) having an emissivity value equal to 0.85. This implies that the material is 85 % efficient at radiating energy.

The thesis of the authors is based on the observation time t as a function (in a first approximation) of the square of the depth z, while the loss of contrast c is proportional to the cube of the depth. In the first case, the thermal diffusivity parameter plays an important role according to Fig. 8. Readers can compare the red dotted oval that surrounds the inspected part in both figures. Finally, Fig. 7j seems to illustrate with a clear contrast the damages discovered in the previous figures. The phasegram identifies the ancient restoration discussed with respect to the NIRR result (Fig. 7b) according to the low inspection frequency.

The lower part of the mantle (Fig. 9a) represents a very different case, since it is a very complex surface composed of concave and convex sections. The NIRR approach (Figs. 9b, c) seems to not be useful in the present case, due to the diffuse damaged area which acts like a scattering surface. However, the most interesting features appear in the concave surfaces (Fig. 9d–f, h–m) such as the dark (Fig. 9d–e, m) or white (Fig. 9f, h–l) spots. They are more or less contrasted in relation to the algorithm applied. A possible explanation of these thermal anomalies could be attributed to the thickness reduction during the manufacturing. On the one hand, they are not present in the PCT result (Fig. 9g) nor in the phasegram (Fig. 9n). On the other hand, the latter result clearly shows some defects, pointed out by red arrows, possibly corresponding to detachments between the terracotta support and the exterior golden layer.

Finally, it is also important to note the ability of the PLST technique to detect a round-shaped feature in a concavity of the mantle, highlighted by a dotted red square in Fig. 9j–l. Although it is not possible to combine this anomaly with a particular type of defect without further micro-chemical analyses [51], its presence excludes the fact that the bright or dark spots located inside the concavities of the mantle are linked to environmental reflections. Since the high-backed chair with arms was fixed to the
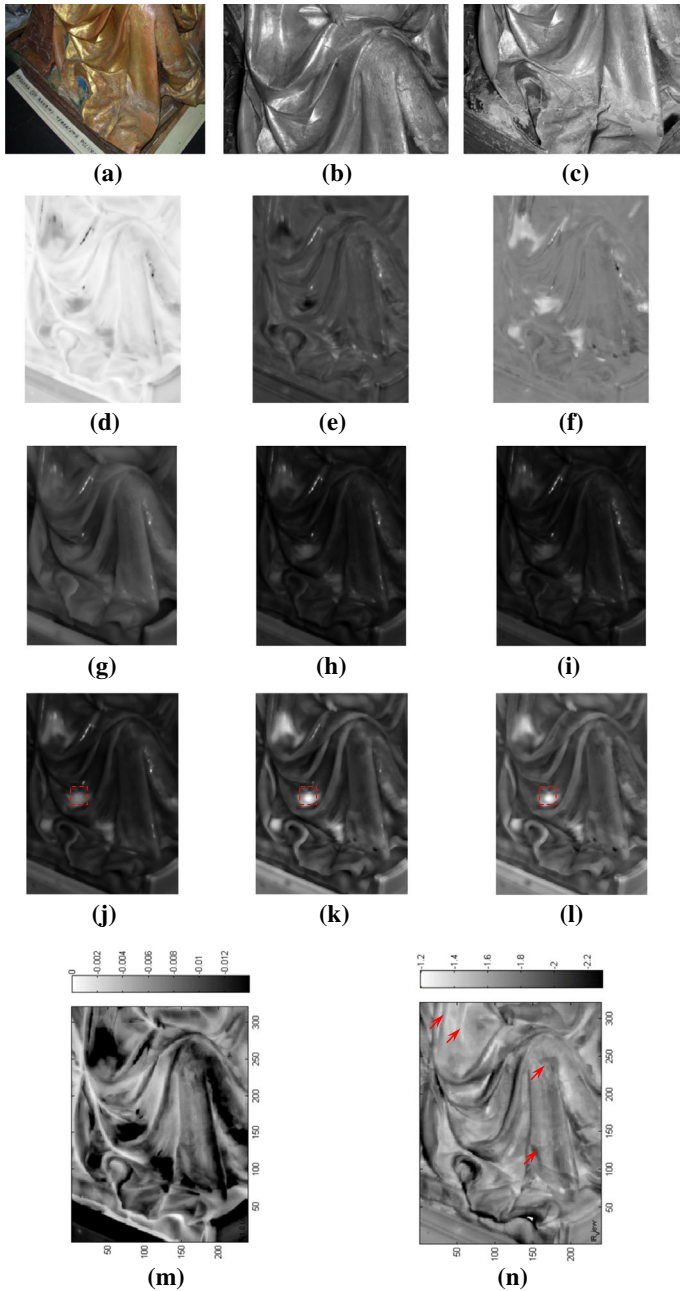
Fig. 9 Our Lady in polychromatic terracotta (detail of the drapery): (a) Photograph, (b) Reflectogram of the upper part of the drapery at 680 nm, (c) Reflectogram of the lower part of the drapery, (d) 1st PLS loading, (e) 2nd PLS loading, (f) 3rd PLS loading, (g) 1st EOF–PCT, (h) 2nd EOF–PCT, (i) 3rd EOF–PCT, (j) Regressed thermal sequences (all components)—50th image, (k) Regressed thermal sequences (all components)—100th image, (l) Regressed thermal sequences (all components)—110th image, (m) TSR, 4th degree, 1st derivative, and (n) PPT, phasegram at $f = 0.0008$ Hz

Before: The *Madonna* brought to light from the debris. It is on a high-backed chair with arms.

After: The *Madonna* during the G8 summit held in L'Aquila (Italy). The right arm is completely detached and preserved in a cavity at the base.

Fig. 10 On the left: The *Madonna* after the recovering from the debris, and on the right: The *Madonna* during the G8 summit. It is possible to notice that the right arm is broken at this stage. The right arm was therefore put in a cavity (an enlargement is shown in this figure) present at the base of the structure

statue, it is possible to assume that the detachment of the arm, probably caused by an impact damage during the transportation, provoked additional internal damage where the thickness of the mantle is thinner, *i.e.*, in the concavities. The comparison among the conservation of the statue before and after the G8 summit held in L'Aquila (Italy) in 2009 clarifies this assumption (Fig. 10). The thermographic measurements were conducted after the G8 summit.

A golden layer upholsters the mantle of *Saint Equizio* (Fig. 11a) similar to that of the statue of the *Madonna*. Unfortunately, the historical photograph (Fig. 11b) does not clarify the state of conservation of the half bust in 1958. However, a pictorial retouching can be identified by comparing the photograph (Fig. 11a) to the NIRR image (Fig. 11c). At the base of this assumption, there is the presence, also in this case, of the red bolo. The reader can note the reddish color which appears on the gilded coating due to the effect of time. As mentioned above, thin layers, opaque to visible light, are often partially transparent to radiation in the 680–2000 nm range. This is our case. The red bolo is strictly connected with the presence of gesso in order to apply the gilded coating as a finishing surface. White gesso reflects infrared rays, but where light-colored portions are present, the reflectance is reduced.
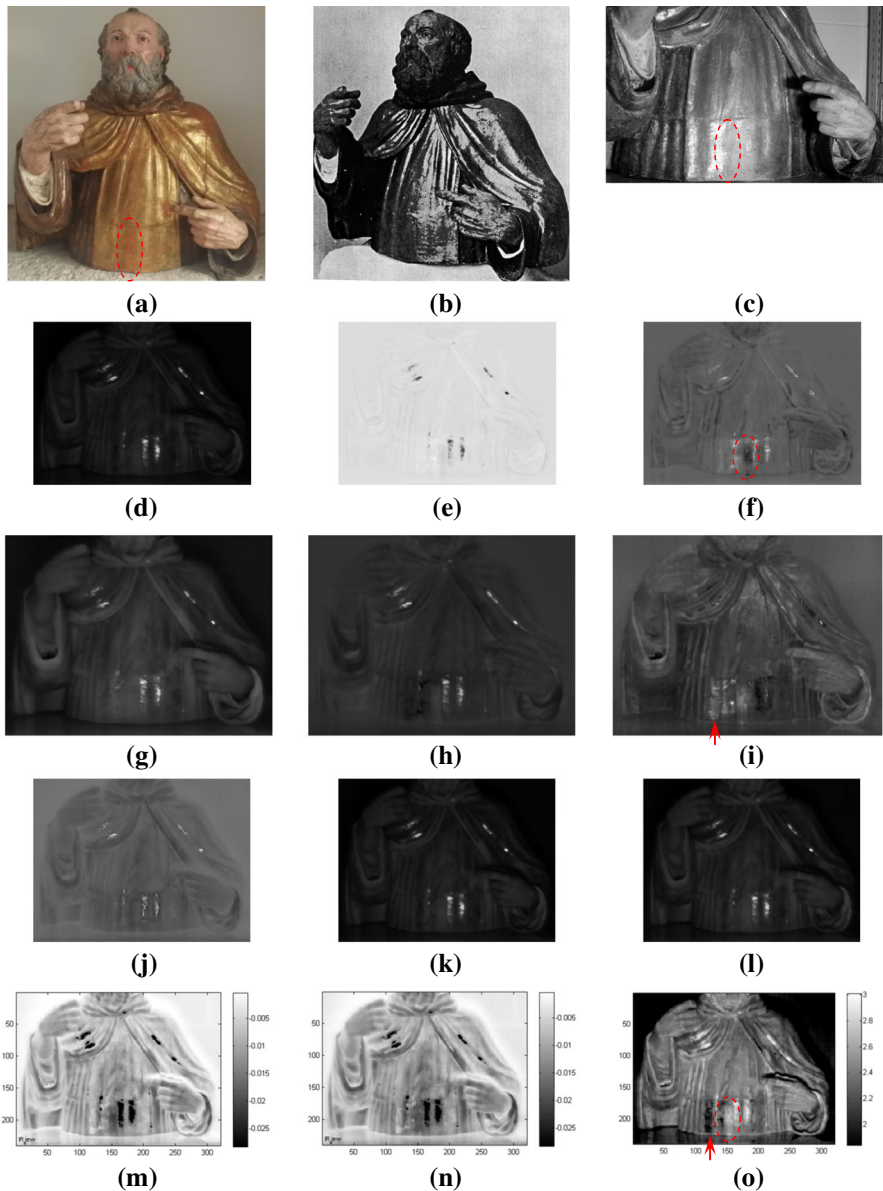
Fig. 11 *Saint Equizio* polychromatic wooden statue: (a) Photograph, (b) Historical photograph, adapted from [13], (c) Reflectogram at 680 nm, (d) 1st PLS loading, (e) 2nd PLS loading, (f) 3rd PLS loading, (g) 1st EOF–PCT, (h) 2nd EOF–PCT, (i) 3rd EOF–PCT, (j) Regressed thermal sequences (all components)—50th image, (k) Regressed thermal sequences (all components)—100th image, (l) Regressed thermal sequences (all components)—110th image, (m) TSR, 4th degree, 1st derivative, (n) TSR, 4th degree, 2nd derivative, and (o) PPT, phasegram at $f = 0.0063$ Hz

The case study of *Saint Equizio* is quite similar to the that of the mantle of the Madonna. Indeed, sub-superficial anomalies located on the more pronounced parts of

the mantle can be retrieved working with different algorithms. Sub-superficial anomalies manifest themselves as white (Fig. 11d, f, g, h, j, k, l, o) or black (Fig. 11e, i, m, n) spots. However, they are located in the same areas. On the one hand, the positions of the defects are not surprising because the statue fell down during the 2009 quake impacting on the debris. On the other hand, taking into account the potentialities of the different algorithms used, these defects cannot be attributed to environmental reflections. It is important to notice that, also in this case, the phasegram (Fig. 11o) reveals the anomaly detected by the NIRR technique (Fig. 11c) due to the selected frequency. It is also important to remember how phasegrams are usually preferred for analysis since they are more tolerant to the nonuniform heating, emissivity variations, and environmental reflections compared to amplitude images [52]. The reflections in this case, as well as in the previous cases analyzed, were minimized by using polystyrene panels mounted around the thermal camera lens, as well as by considering the reflectance curve at 45° with an in-going direction of the IR rays originating from the lamp (Fig. 4b). This is similar to the PLST result shown in Fig. 11f, because the emissivity variation was removed at the specific frequency, as suggested in [53]. This led to a remarkable improvement in defect detectability. In both cases, the defect is surrounded by a red dotted oval.

The PPT combined with PCT leads to a different result and displays the presence of a persistent environmental reflection on the left side of the mantle. The position of the thermal camera, as well as the complex shape of that part, leads to this unwanted effect. It is also noticeable looking at the raw thermograms. Readers can refer to the red arrows placed in both figures (Fig. 11i, o).

8 Conclusions

On the basis of the combination of *nondestructive testing* and *cultural heritage* in order to solve decay problems [54], the present work describes a comparative application between advanced techniques applied to near- and far- infrared images. They are able to detect superficial and sub-superficial defects in polychromatic statues, in which external layers are applied with the purpose of covering different supports. On the one hand, the dynamic heat transport caused by variations in paint thickness was taken into account using thermographic observations to track differences concerning the thermal imprints in time. On the other hand, the potentiality to reveal defects beneath superficial golden coatings was investigated. In general, the results appear in good agreement, although an integrated use between the previously mentioned techniques is suggested in order to avoid *false alarms* during the defect detection. The selected parameters for infrared imaging can be determined only by a combination of theoretical study and experimental research.

It is important to point out that it is much more complicated to provide conclusions without the possibilities of manually handling the samples—considering the importance of the artworks under inspection—with the aim to perform chemical analysis [55] in laboratory.

The reflectographic technique combined with the thermographic technique and a solid knowledge of the physical concepts related to the CH field provided, in the present

case, an important improvement toward distinguishing between environmental reflections, emissivity variations, sub-superficial defects, and reduction in the thicknesses of the materials during manufacturing [56].

As a future perspective of the present work, the authors would like to inspect additional statues having different coatings. For example, silver and copper coatings may be of interest to be inspected, as well as the use of mid-infrared cameras with the aim to compare the results obtained with the present ones. In order to optimize the thermal stimulus to be provided on the surfaces in terms of both duration and type, a numerical simulation studied *ad hoc* in Comsol Multiphysics® environment will be used. The latter will also be useful to foresee the behavior of each algorithm applied herein thanks to the use of a specific script written in Matlab® environment focused on thermographic simulations. In this way, potential shortcomings and workable solutions will be considered before starting the experimental approach. Completing the thermal and nonthermal maps of the more reflective pigments, it will be possible to move the attention on additional CH objects having simpler surface but a more variegate palette of colors. This is the case of the polyptychs of very important art masters, such as Taddeo Gaddi, Simone Martini, and Giovanni de Ponte, which could benefit by the integrated approach proposed in this work and in the future.

References

1. I. Crina Anca Sandu, M.H. de Sá, M.C. Pereira, Surf. Interface Anal. **43**, 1134 (2011)
2. E. Hecht, A. Zając, *Optics*, 4th edn. (Pearson Education Limited, Hoboken, 2001)
3. R.L. Feller, *Artists Pigments: A Handbook of Their History and Characteristics*, vol. 1 (Cambridge University Press, London, 1987)
4. H.A. Gardner, G.G. Sward, *Paint Testing Manual*, 13th edn. (ASTM International, Philadelphia, 1972)
5. R.J. Gettens, G.L. Stout, *Painting Materials: A Short Encyclopedia* (Dover Publications, London, 2011)
6. A.P. Laurie, *The Painters Methods and Materials* (Dover Publications, New York, 1988)
7. S.A. Humphrey, P.J. Laden, *Gold Bronze Pigment in Pigments Handbook. Properties and Economics*, vol. 1 (Wiley, New York, 1988), pp. 803–810
8. J.V. Koleske, *Paint and Coating Testing Manual (Fourteenth Edition of the Gardner-Sward Handbook)*, ASTM Manual Series: MLN 17, Philadelphia (PA) (1995)
9. H.S. Carslaw, J.C. Jaeger, *Conduction of Heat in Solids*, 2nd edn. (Clarendon Press, Oxford, 1959)
10. Y.V. Petrov, N.A. Inogamov, K.P. Migdal, Two-temperature heat conductivity of gold, in *Proceedings of Progress in Electromagnetics Research Symposium, Prague, Czech Republic* (2015)
11. J.R.J. Van Asperen de Boer, Appl. Opt. **7**, 1711 (1968)
12. X.P.V. Maldague, *Theory and Practice of Infrared Technology for Nondestructive Testing* (Wiley, New York, 2001)
13. A.M. Reggiani, Recuperata statua Terracotta attribuita a Saturnino Gatti, L'Editoriale online (2009). http://www.leditoriale.com/index.php?page=turismo&turismo=803. Accessed 21 Apr 2016

14. E. Santilli, Silvestro di Giacomo da Sulmona, detto Silvestro Aquilano (ca. 1450–1504). Scultore, pittore, figulo, architetto, Regione Abruzzo—Assessorato alla Cultura (2012). file:///C:/Users/Utente/Downloads/SILVESTRObiografia1.pdf. Accessed 21 Apr 2016
15. P. Conti, La Madonna scampata al sisma perde pezzi alla mostra 'per' il sisma, Corriere della sera.it (2009). http://www.corriere.it/cronache/09_settembre_24/conti-madonna-500-sisma_61df05cc-a8e1-11de-aaa2-00144f02aabc.shtml. Accessed 21 Apr 2016
16. M. Corridore, Statua della Madonna di Saturnino Gatti ritrovata a Londra, Il Centro (2016). http://ilcentro.gelocal.it/laquila/cronaca/2016/04/09/news/statua-della-madonna-di-saturnino-gatti-ritrovata-a-londra-1.13270211. Accessed 21 Apr 2016
17. F. Verlengia, Pompeo Cesura. Pittore aquilano del '500, Stabilimento Poligrafico Editoriale Amoroso, Pescara (1958)
18. F. Mercuri, N. Orazi, U. Zammit, S. Paoloni, M. Marinelli, P.P. Valentini, e-PS **9**, 84 (2012)
19. S. Sfarra, C. Ibarra-Castanedo, S. Ridolfi, G. Cerichelli, D. Ambrosini, D. Paoletti, X. Maldague, Appl. Phys. A. Mater. **115**, 1041 (2014)
20. B.-H. Mevik, R. Wehrens, J. Stat. Softw. **18**, 1 (2007)
21. N. Rajic, Compos. Struct. **58**, 521 (2002)
22. P. Bison, A. Bortolin, G. Cadelano, G. Ferrarini, F. López, X. Maldague, Evaluation of frescoes detachments by partial least squares thermography, in *Proceedings of the International Conference on Quantitative Infrared Thermography (QIRT)* (2014)
23. P. Bison, A. Bortolin, G. Cadelano, G. Ferrarini, F. López, X. Maldague, Comparison of image processing techniques for the on-site evaluation of damaged frescoes, in *Proceedings of SPIE—The International Society for Optical Engineering, Thermosense XXXVI* (2014)
24. F. López, C. Ibarra-Castanedo, V. de Paulo Nicolau, X. Maldague, NDT&E Int. **66**, 128 (2014)
25. X. Maldague, S. Marinetti, J. Appl. Phys. **79**, 2694 (1996)
26. S.M. Shepard, J.R. Lhota, B.A. Rubadeux, D. Wang, T. Ahmed, Opt. Eng. **42**, 1337 (2003)
27. S.M. Shepard, Mater. Eval. **65**, 690 (2007)
28. D.L. Balageas, J.M. Roche, F.-H. Leroy, W.-M. Liu, A.M. Gorbach, Biocybern. Biomed. Eng. **35**, 1–9 (2015)
29. M.T. Klein, C. Ibarra-Castanedo, X. Maldague, A. Bendada, A straightforward graphical user interface for basic and advanced signal processing of thermographic infrared sequences, in *Proceedings of SPIE—The International Society for Optical Engineering, Thermosense XXX* (2008)
30. S. Sfarra, C. Ibarra-Castanedo, D. Paoletti, X. Maldague, Mater. Eval. **71**, 561 (2013)
31. A. Bayler, A. Schier, G.A. Bowmaker, H. Schmidbaur, J. Am. Chem. Soc. **188**, 7006 (1996)
32. P.K. Mehrotra, R. Hoffmann, Inorganic Chem. **17**, 2187 (1978)
33. H.E. Merwin, Optical properties and theory of color of pigments and paints, in *Proceedings of the American Society for Testing Materials XVII* (1917)
34. A.D. Raki?, A.B. Djurišic, J.M. Elazar, M.L. Majewski, Appl. Opt. **37**, 5271 (1998)
35. C. Chiojdeanu, D. Cristea Stan, B. Constantinescu, Roman. Rep. Phys. **63**, 685 (2011)
36. G. Hanlon, Why some paints are transparent and others opaque. Natural Pigments (2013). http://www.naturalpigments.com/art-supply-education/transparent-opaque-paints/. Accessed 21 April 2016
37. M. Gimeno Concepción, The chemistry of gold, in *Modern Supramolecular Gold Chemistry: Gold-Metal Interactions and Applications*, ed. by A. Laguna (Wiley-VCH, New York, 2008), pp. 1–64
38. F. López, X. Maldague, C. Ibarra-Castanedo, Opto-Electron. Rev. **22**, 245 (2014)
39. S. Sfarra, C. Ibarra-Castanedo, D. Ambrosini, D. Paoletti, A. Bendada, X. Maldague, Arab. J. Sci. Eng. **39**, 3461 (2014)
40. P. Kubelka, F. Munk, Zeits. f. Techn. Physik **12**, 593 (1931)
41. P. Miracola, Il restauro di due opera in terracotta dipinta: Il presepe di Santa Maria del Ponte e la Madonna di Collemaggio, Gangemi Ed., Italy (2015)
42. N. Penni, *The Materials of Sculpture* (Yale University Press, London, 1993)
43. R. Mayer, *The Artist's Handbook of Materials and Techniques*, 5th edn. (Faber & Faber, London, 1991)
44. C. Ibarra-Castanedo, Ph.D. thesis, Laval University, Quebec City, QC, Canada (2005). http://www.theses.ulaval.ca/cocoon/meta/2005/23016.xml. Accessed 1 June 2017
45. S. Sfarra, P. Theodorakeas, C. Ibarra-Castanedo, N.P. Avdelidis, D. Ambrosini, E. Cheilakou, D. Paoletti, M. Koui, A. Bendada, X. Maldague, Int. J. Thermophys. **36**, 3051 (2015)
46. C. Ibarra-Castanedo, S. Sfarra, D. Ambrosini, D. Paoletti, A. Bendada, X. Maldague, QIRT J. **5**, 131 (2008)

47. C. Ibarra-Castanedo, S. Sfarra, D. Ambrosini, D. Paoletti, A. Bendada, X. Maldague, QIRT J. **7**, 85 (2010)
48. C. Ibarra-Castanedo, S. Sfarra, D. Paoletti, A. Bendada, X. Maldague, Nondestructive testing of externally reinforced structures for seismic retrofitting using flax fiber reinforced polymer (FFRP) composites, in *Proceedings of SPIE—The International Society for Optical Engineering, Thermosense XXXV* (2013)
49. F. López, V.P. Nicolau, C. Ibarra-Castanedo, S. Sfarra, X. Maldague, Comparative study of thermographic signal reconstruction and partial least squares thermography for the detection and evaluation of subsurface defects, in *Proceedings of the International Conference on Quantitative Infrared Thermography (QIRT)* (2014)
50. S. Sfarra, C. Ibarra-Castanedo, D. Ambrosini, D. Paoletti, A. Bendada, X. Maldague, J. Nondestruct. Eval. **33**, 358 (2014)
51. M. Tortora, S. Sfarra, M. Chiarini, V. Daniele, G. Taglieri, G. Cerichelli, Appl. Surf. Sci. **387**, 971 (2016)
52. Y. Duan, S. Huebner, U. Hassler, A. Osman, C. Ibarra-Castanedo, X.P.V. Maldague, Infr. Phys. Technol. **60**, 275 (2013)
53. R. Yang, Y. He, B. Gao, G.Y. Tian, Appl. Phys. Lett. **105**, 184103 (2014)
54. G. Taglieri, V. Daniele, G. Rosatelli, S. Sfarra, M.C. Mascolo, C. Mondelli, J. Cult. Herit. **25**, 135 (2017)
55. R. Cesareo, G. Buccolieri, A. Castellano, R.T. Lopes, J.T. De Assis, S. Ridolfi, A. Brunetti, A. Bustamante, X-Ray Spectrom. **44**, 233 (2015)
56. H. Zhang, S. Sfarra, K. Saluja, J. Peeters, J. Fleuret, Y. Duan, H. Fernandes, N. Avdelidis, C. Ibarra-Castanedo, X. Maldague, J. Nondestruct. Eval. **36**, 1 (2017)